Supporting Information for

Why poorly conductive Bi@UiO-MOF can catalyze CO_2 electroreduction?

Xinru He,[a] Ying Guo,[b] Jingzheng Zhang,[c] Shuangli Yang,[a] Jiawei Chen,[a] Shurong Li,[a] Shunji Xie,[a] Ye Wang,[a] Cheng Wang*[a]

[a] State Key Laboratory of Physical Chemistry of Solid Surfaces, iChem, Innovation Laboratory for Sciences and Technologies of Energy Materials of Fujian Province (IKKEM), College of Chemistry and Chemical Engineering, Xiamen University, Xiamen 361005, P. R. China.

[b] School of Chemistry and Chemical Engineering, Northwestern Polytechnical University, Xi'an 710129, P. R. China.

[c] Green Catalysis Center, and College of Chemistry, Zhengzhou University Zhengzhou 450001, P. R. China.

1. Experimental Procedures

1.1 General Experimental

Reagents were commercially available and used without further purification unless otherwise noted. Distilled water with the specific resistance of 18.2 MΩ · cm was obtained from Direct-Q 3UV water purification system.

Powder X-ray diffraction (PXRD) was carried out on Rigaku DMax-γA rotation anode X-ray diffractometer equipped with graphite monochromatized Cu Ka radiation (γ = 1.54 Å). Transmission electron microscopy (TEM) and EDX mapping were acquired on Phillips Analytical FEI Tecnai F30 electron microscope operated at an electron acceleration voltage of 300 kV. Thermogravimetric analysis (TGA) was performed in air using Shimadzu TGA-50 equipped with an aluminum pan and heated at a rate of 5°C per minute. FT-IR spectrum were obtained on Nicolet iS50 FTIR spectrometer. Scanning electron microscopy (SEM) and EDX mapping were obtained on ZEISS sigma. The XPS measurements were conducted using PHI Quantum 2000 equipment. Inductively coupled plasma-mass spectrometry (ICP-MS) analyses were performed on ELAN ICP-DRC-qMS (PerkinElmer, SCIEX, Canada) instrument equipped with a concentric pneumatic nebulizer (Meinhard) and a cyclonic spray chamber. Nitrogen sorption measurements were obtained on Automatic physical adsorption instrument ASAP 2460 at 77 K. The samples were prepared at 150 °C in vacuum for 6 h. The surface area was calculated using Brunauer-Emmett-Teller (BET) method in the range of P/P_0 = 0.0-1. Pore size was evaluated by the Horvath-Kawazoe method.

1.2 Electrochemical Experiments

All electrochemical measurements were performed using a three-electrode system and an electrochemical workstation (CHI660E). Electroreduction CO_2 experiments were performed in an H-type cell at room temperature, and electrolyte was CO_2-saturated 0.1 M $KHCO_3$ with pH of 6.8. The reference electrode was saturated Ag/AgCl electrode, the counter electrode was Pt

wire. The cathode was separated from the anode compartment by a proton exchange membrane (Nafion 117). All potentials were converted to reversible hydrogen electrode (RHE) scale using E (V *vs.* RHE) = E (V *vs.* Ag/AgCl) + 0.21 V + 0.0591 V×pH. Typically, 3 mg of catalysts were dispersed in 1.2 mL of isopropanol by sonicating for 10 min to form a homogeneous ink，then 400 μL of the suspension were drop-casted on the hydrophobic carbon cloth.

Linear sweep voltammetry (LSV) and Cyclic voltammograms (CV) at a scan rate of 50 mV s^{-1} was measured in a CO_2-saturated 0.1 M $KHCO_3$ (pH 6.8) and N_2-saturated 0.1 M KH_2PO_4/K_2HPO_4 at room temperature on a glass carbon electrode (GCE). Flow cell measurements were performed in a three-electrode cell reactor. A gas diffusion layer (GDL) as working electrode, a proton exchange membrane (Nafion 117) separated the anode compartment and cathode compartment. The saturated Ag/AgCl electrode and $IrO_2 \cdot xH_2O$ were respectively used as the reference and counter electrode. The size of the cathode window was 0.4 x 2.0 cm^2. The flow rate of CO_2 gas was 24 mL min^{-1}, electrolyte was circulated through the cathode compartment at a rate of 11 mL min^{-1}. The cathode electrolyte was 0.1 M $KHCO_3$ + 0.9 M KCl. The anode electrolyte was 1 M $KHCO_3$. Typically, 5.3 mg of catalysts were dispersed in 0.4 mL of isopropanol by ultrasonicating for 30 min to form a homogeneous ink，then added 20 μL 5% Nafion neutral solution and ultrasonication for another 20 min. 200 μL of the catalysts ink was drop-casted on the GDL (0.5 mg cm^{-2}). The iR compensation level was set at 80% in flow cell measurements.

1.3 Products analysis

Gas phasic products (H_2, CO) were quantified by online gas chromatography with a flame ionization detector (FID) and a thermal conductivity detector (TCD). The liquid products were detected by proton nuclear magnetic resonance (^{1}H NMR) spectra (Bruker AVANCEAV III 500 MHz). The ^{1}H-NMR spectrum was measured with water suppression using a pre-saturation sequence. The electrolyte (500 μL) was mixed with 100 μL deuterated water (D_2O), and 0.02 μL dimethyl sulfoxide (DMSO) as an internal standard.

1.4 Electrical conductivity measurements

I-V curves were measured by Keithley 2450 source meter. The powders of MOF were pressed into pellets. The thickness *l* and area *S* of each sample was measured for the electrical conductivity calculation. The resistance *R* of each sample was obtained from the slope of the *I-V* curve. The electrolyte solution (CO_2-saturated 0.1 M $KHCO_3$) resistance R_s was obtained by immersing the pair of electrodes without the MOF pellet in the electrolyte solution and keeping the distance between the electrodes the same as the thickness of the MOF pellet. The resistance R_{ct} of MOF in CO_2-saturated 0.1 M $KHCO_3$ was calculated by the following equation

$$\frac{1}{R} = \frac{1}{R_S} + \frac{1}{R_{ct}}$$

Where *R* is the measured resistance with the MOF pellet in between the electrodes immersed in the electrolyte solution

The resistance of the MOF without electrolyte was measured with dry MOF pellet.

The electrical conductivity σ was calculated by the following equation

$$\sigma = \frac{l}{R_{ct} \times S}$$

where l is the thickness of the MOF pellet, and S is the area of the pellet

The total current density through the MOF is calculated by

$$j = \frac{I}{geometric\ area}$$

where I is the total current

$$j_0 = \frac{j}{roughness\ factor}$$

j_0 is the current density on the MOF catalyst, and the roughness factor of the carbon cloth was calculated from the ratio of electrochemical active surface area ECSA over the geometric area. The ECSA was caculated from double layer capcitance measurement.

2. Catalyst preparation

2.1 Synthesis of UiO-66-SH:

The synthesis of UiO-66-SH framework followed the procedures in previous work. A mixture of $ZrCl_4$ (96 mg), 2,5-dimercapto-1,4-benzenedicarboxylic acid (BDC-$(SH)_2$, 95 mg) and acetic acid (3.76 mL) were dissolved in DMF (16 mL) in a Schlenk tube. Then the tube was evacuated and refilled by Ar for 3 times. The tube was then capped tightly and kept at 120 ℃ for 24 h. After cooling to the room temperature, the solid powder was collected by centrifugation. After washed with DMF for several times until the supernatant solution was clarified, then solvent exchanged with acetone for one day. Vacuum dry the collected yellow powder.

2.2 Synthesis of UiO-66-S-Bi:

A mixture of UiO-66-SH and $Bi(NO_3)_3 \cdot 5H_2O$ (0.37 equiv.to S) was dispersed in H_2O in a Pyrex vial and kept stirring overnight. The sample was collected by centrifugation, and washed with water five times then soaked in water for a day and centrifuged to change water three times. The collected orange powder was then dried under vacuum.

2.3 Synthesis of UiO-66-SH@UiO-66(Hf):

A precursor solution of UiO-66(Hf) was prepared as follow: $HfCl_4$ (20.6mg), BDC (12.5 mg) and formic acid (300 μL) were dissolved in 750 μL DMF. Then 2.7mg of UiO-66-SH was dispersed in 750 μL of DMF and mixed with 80.6 μL of precursor solution in Pyrex vial. The vials were kept at 120℃ for 7h. After that, the yellow product was collected by centrifugation and washed thrice with DMF. Finally, the MOF was immersed in acetone for one day for solvent exchange. The collected yellow powder was then dried under vacuum.

2.4 Synthesis of UiO-66-S-Bi@UiO-66(Hf):

A mixture of UiO-66-SH@UiO-66(Hf) and $Bi(NO_3)_3 \cdot 5H_2O$ (0.37 equiv.to S) was dispersed in H_2O in a Pyrex vial and kept stirring overnight. The sample was collected by

centrifugation and washed with water five times before soaked in water for one day and centrifuged to change water three times. The collected orange powder was then dried under vacuum.

3. Supplementary Data

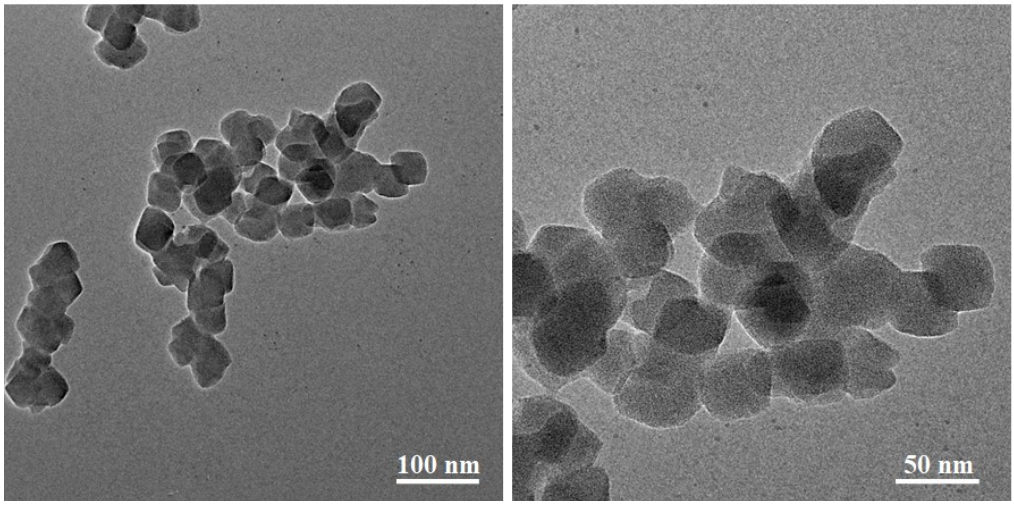

Figure S1. TEM images of UiO-66-SH.

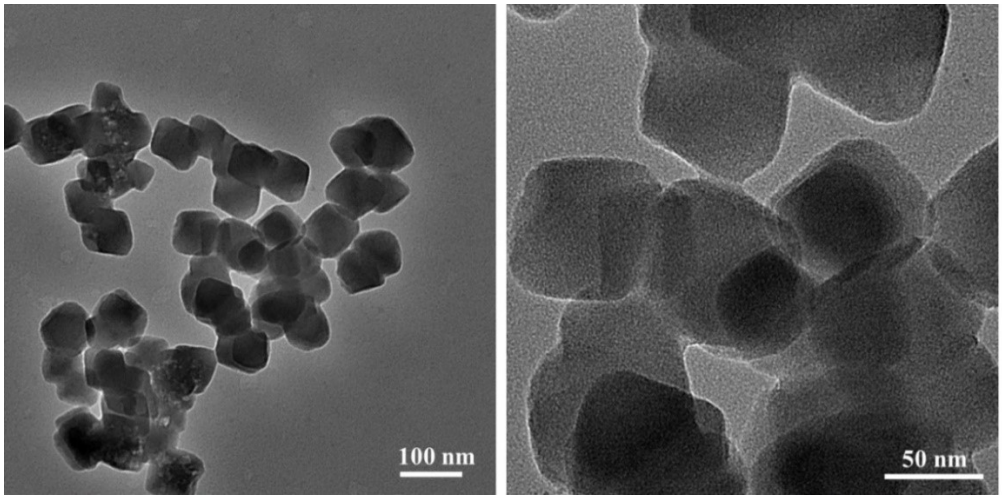

Figure S2. TEM images of UiO-66-S-Bi.

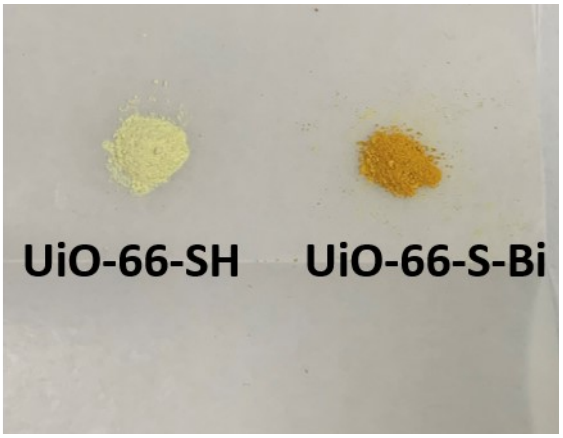

Figure S3. Photos of UiO-66-SH and UiO-66-S-Bi.

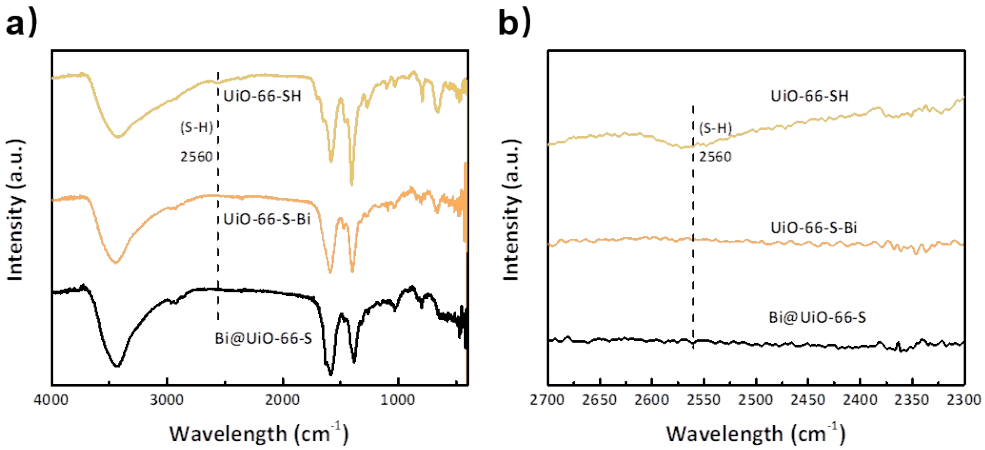

Figure S4. a) FT-IR spectra of UiO-66-SH, UiO-66-S-Bi and the sample after electrolysis. b) The enlarged image of Fig 4a.

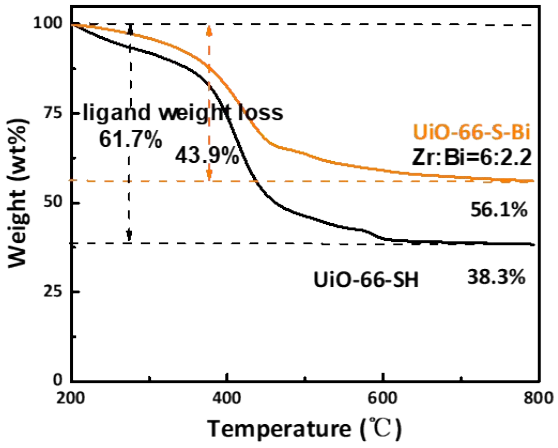

Figure S5. TGA plot of UiO-66-SH and UiO-66-S-Bi.

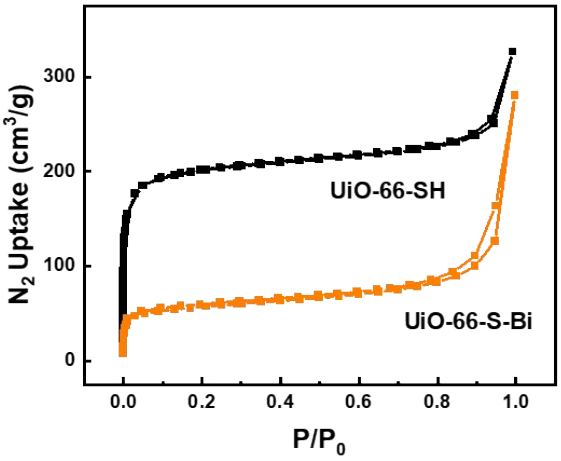

Figure S6. Nitrogen sorption isotherms (77K) of UiO-66-SH and UiO-66-S-Bi.

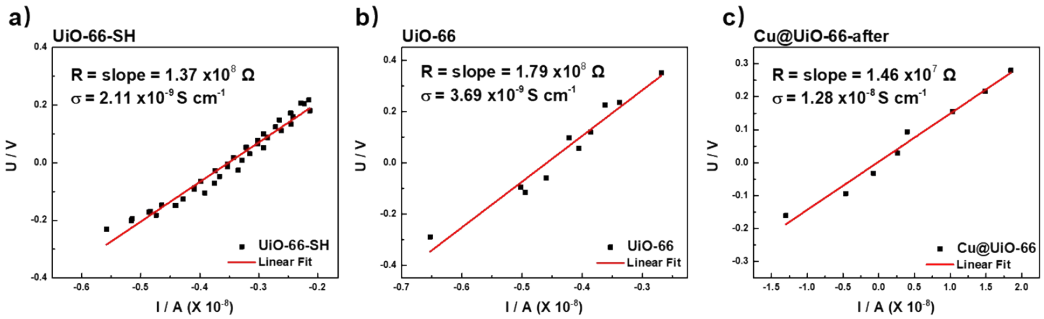

Figure S7. Electrical conductivity measurements for UiO-66-SH (a), UiO-66 (b) and Cu@UiO-66 after electrolysis (c).

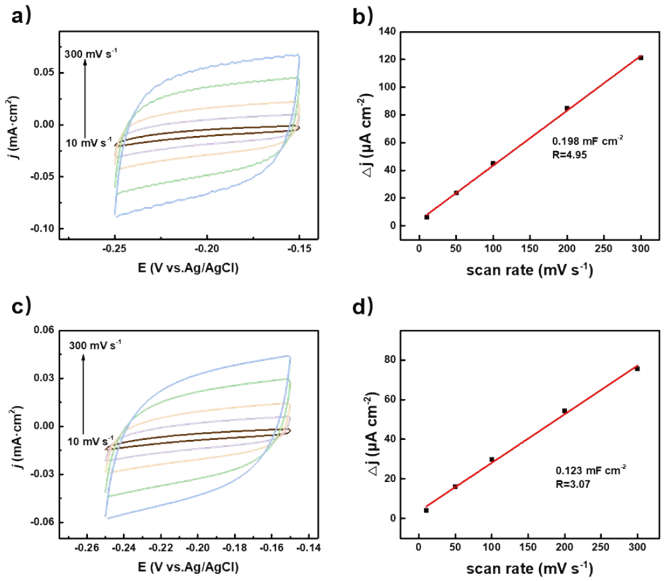

Figure S8. a) Cyclic voltammograms (CV) curves of oxidized carbon cloth. b) Double-layer capacitance (Cdl) of oxidized carbon cloth. c) Cyclic voltammograms (CV) curves of oxidized gas

diffusion layer. d) Double-layer capacitance (Cdl) of oxidized gas diffusion layer.

Note that we need to oxidize the carbon cloth to make it hydrophilic for the measurement of ECSA, otherwise water cannot wet the carbon cloth and leave small bubbles in the carbon cloth that leads to significant underestimation of the ECSA.

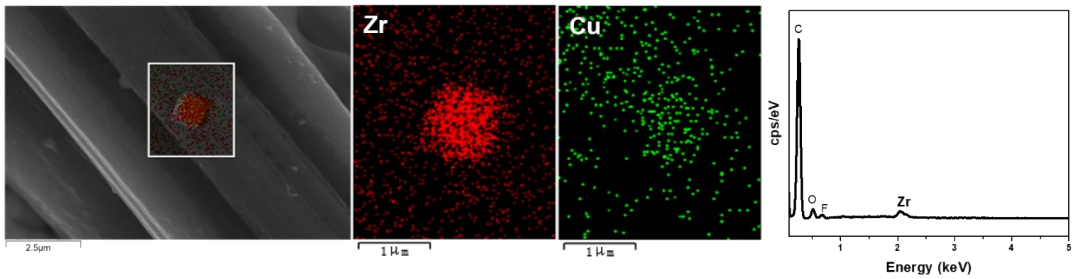

Figure S9. SEM images and EDX mapping of Zr (red) and Cu (green) in UiO-66 with 0.5 mM $CuSO_4$ added in the electrolyte without electrolysis.

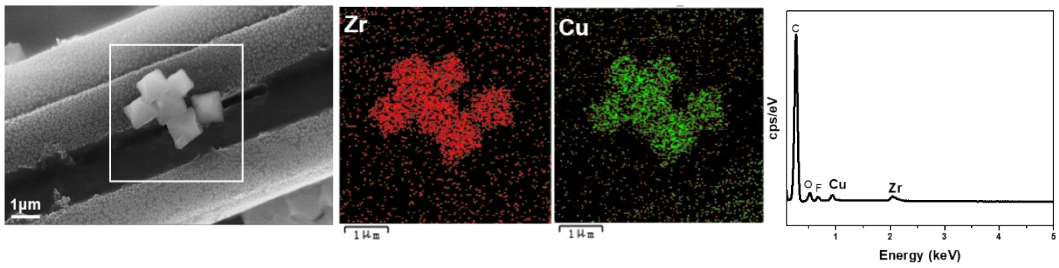

Figure S10. SEM images and EDX mapping of Zr (red) and Cu (green) in UiO-66 with 0.5 mM $CuSO_4$ added in electrolyte after electrolysis at 0.5 V *vs.* RHE.

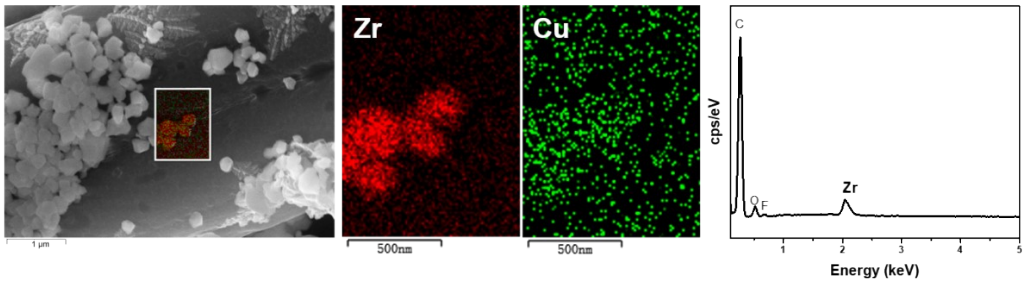

Figure S11. SEM images and EDX mapping of Zr (red) and Cu (green) in ZrO_2 with 0.5 mM $CuSO_4$ added in electrolyte after electrolysis at 0.5 V *vs.* RHE.

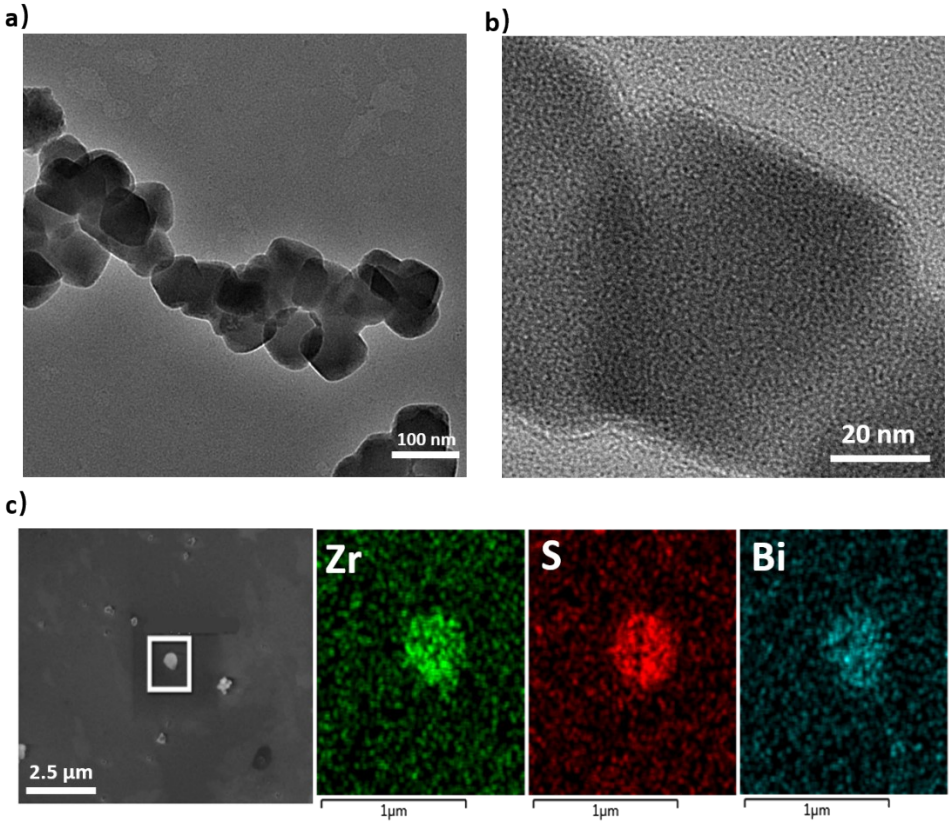

Figure S12. a, b) TEM images of UiO-66-S-Bi after electrolysis (denoted Bi@UiO-66-S). c) SEM images and EDX mapping of Bi@UiO-66-S, Zr (green), S (red) and Bi (blue).

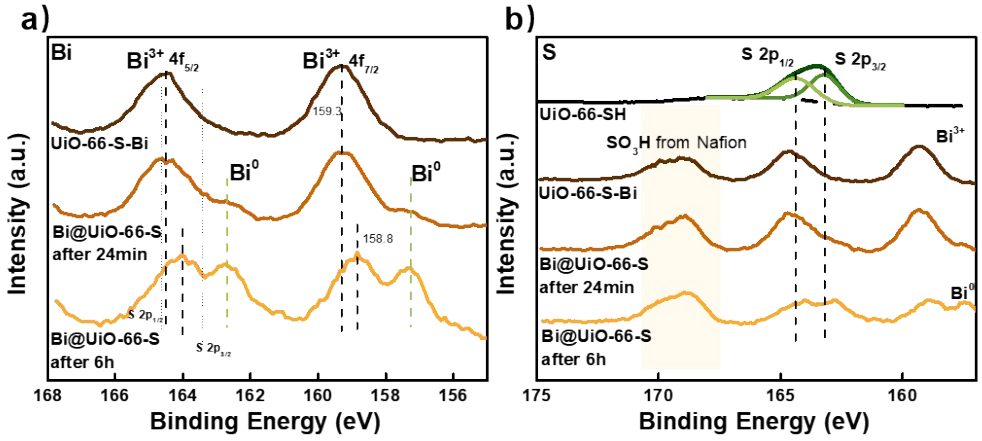

Figure S13. a) *ex-situ* XPS spectra of Bi 4f for UiO-66-S-Bi and the sample after electrolysis (denoted as Bi@UiO-66-SH, the samples were put under nitrogen protection in the whole process of sample transfer). Since the binding energy of S 2p coincides with Bi $4f_{5/2}$, the valence state of Bi is determined by Bi $4f_{7/2}$. b) *ex-situ* XPS spectra of S 2p for the same sample with a) and UiO-66-SH.

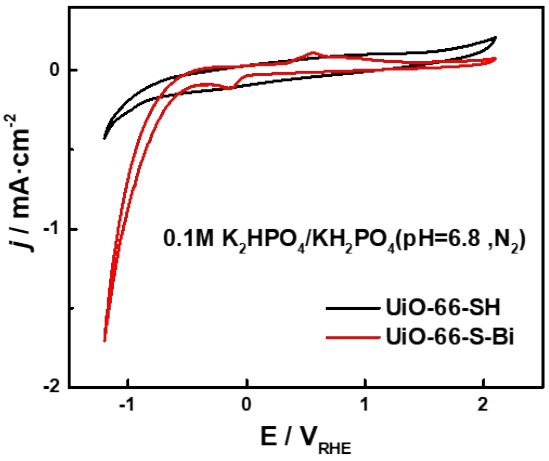

Figure S14. CV curves of UiO-66-SH and UiO-66-S-Bi in N_2-saturated 0.1 M KH_2PO_4/K_2HPO_4 buffer solution (pH = 6.8).

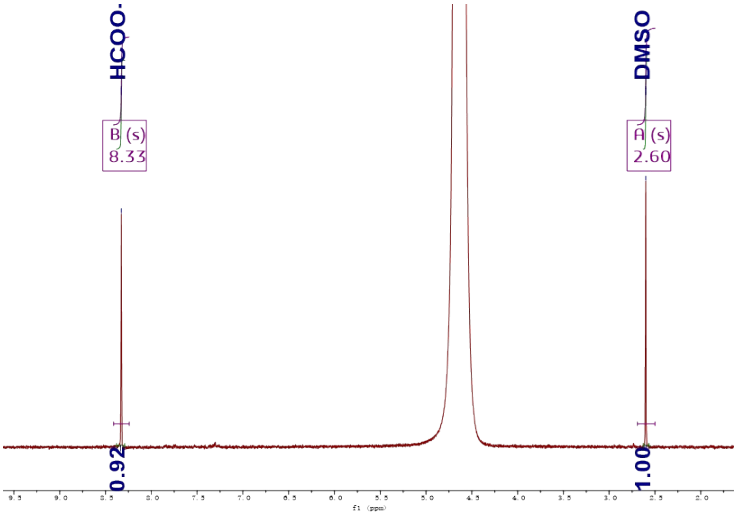

Figure S15. A typical ^{1}H-NMR spectrum of 0.1 M $KHCO_3$ electrolyte after electrocatalytic CO_2 reduction with the UiO-66-S-Bi catalyst.

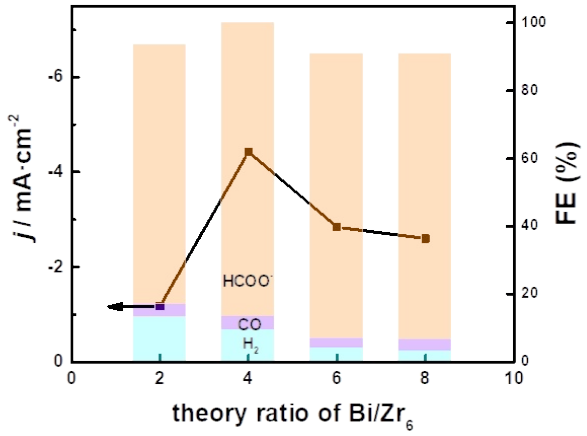

Figure S16. Current densities and Faradaic efficiencies of electrocatalytic CO_2 reduction with different theoretical Bi loading amount at -1.1 V *vs.* RHE.

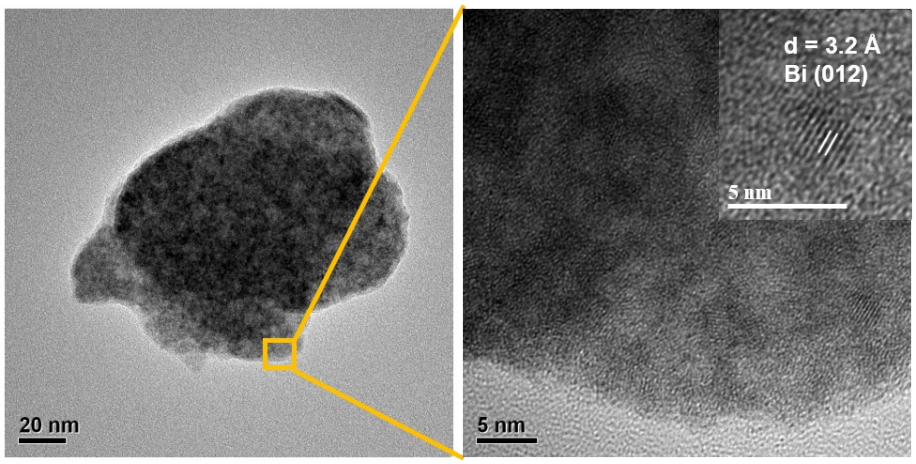

Figure S17. HRTEM images of Bi@UiO-66-S.

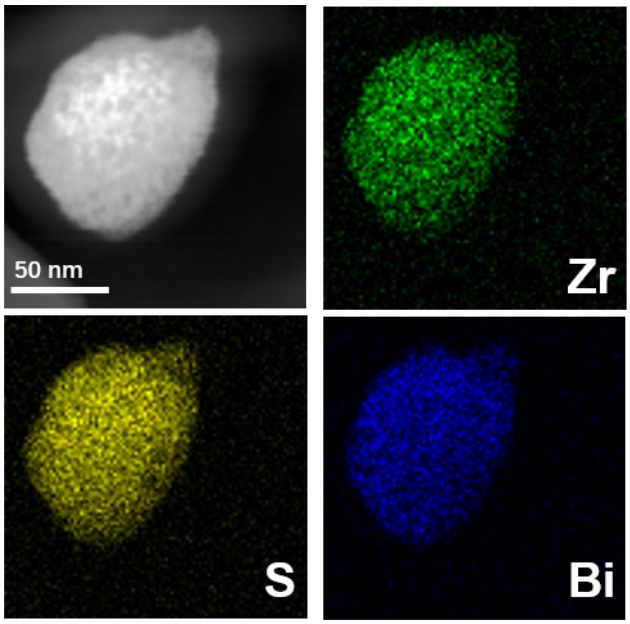

Figure S18. High-angle annular dark-field image and EDX mapping of Zr (green), S (yellow) and Hf (navy blue) in Bi@UiO-66-S.

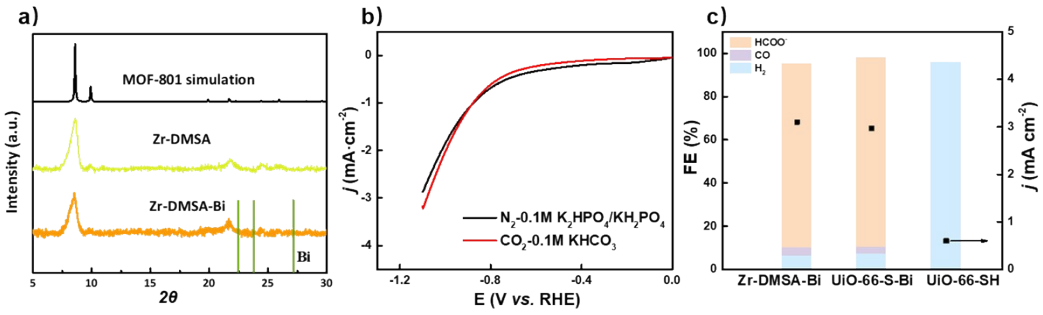

Figure S19. a) PXRD patterns of the Zr-DMSA, Zr-DMSA-Bi and the simulation of MOF-801. b) LSV curves of the Zr-DMSA-Bi in N_2-saturated 0.1 M KH_2PO_4/K_2HPO_4 buffer solution (pH=6.8) and CO_2-saturated 0.1 M $KHCO_3$ solution (pH=6.8). c) FE and current density of electrocatalytic CO_2 reduction for Zr-DMSA-Bi, UiO-66-S-Bi and UiO-66-SH at-1.1 V *vs.* RHE in CO_2-saturated 0.1 M $KHCO_3$ solution (pH = 6.8).

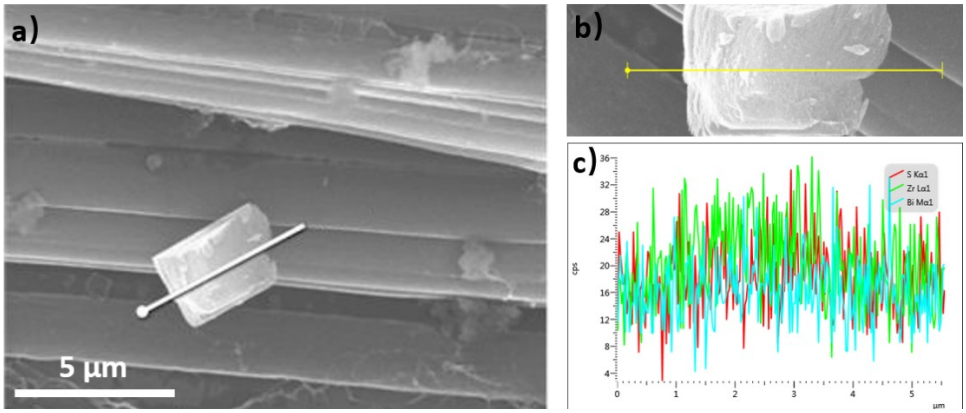

Figure S20. a, b) Cross section SEM images of UiO-66-S-Bi. c) Distribution of Zr and Bi obtained by EDX line scan on a section of UiO-66-S-Bi.

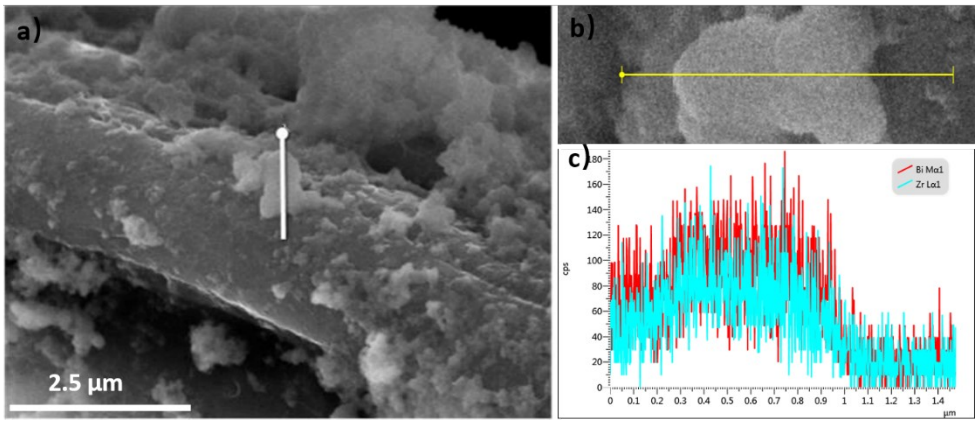

Figure S21. a, b) Cross section SEM images of Bi@UiO-66-S. c) Distribution of Zr and Bi obtained by EDX line scan on a section of Bi@UiO-66-S.

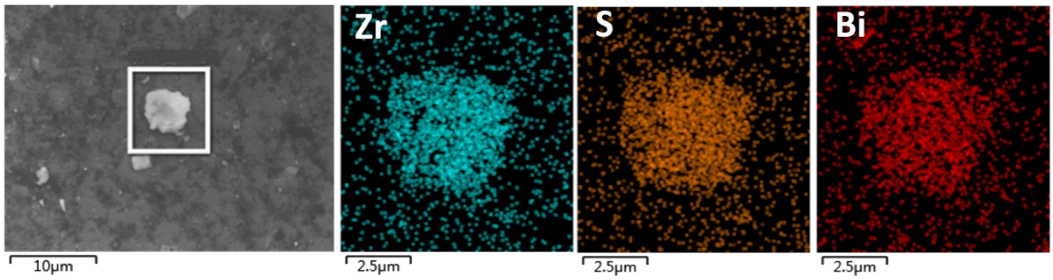

Figure S22. SEM images and EDX mapping of Zr (blue), S (orange) and Bi (red) in UiO-66-S-Bi after long-term electrolysis.

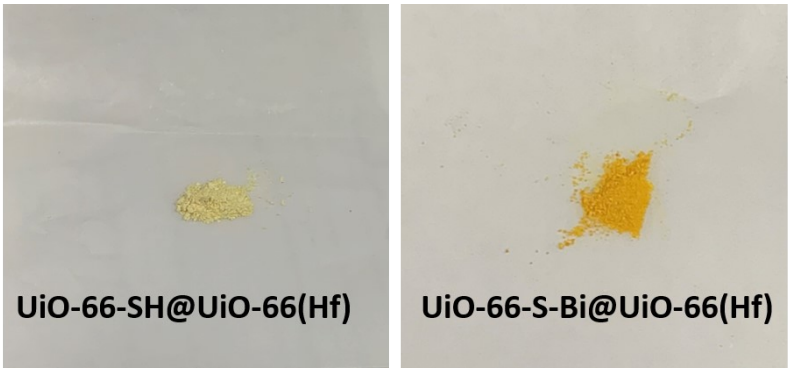

Figure S23. Photos of UiO-66-SH@UiO-66(Hf) and UiO-66-S-Bi@UiO-66(Hf).

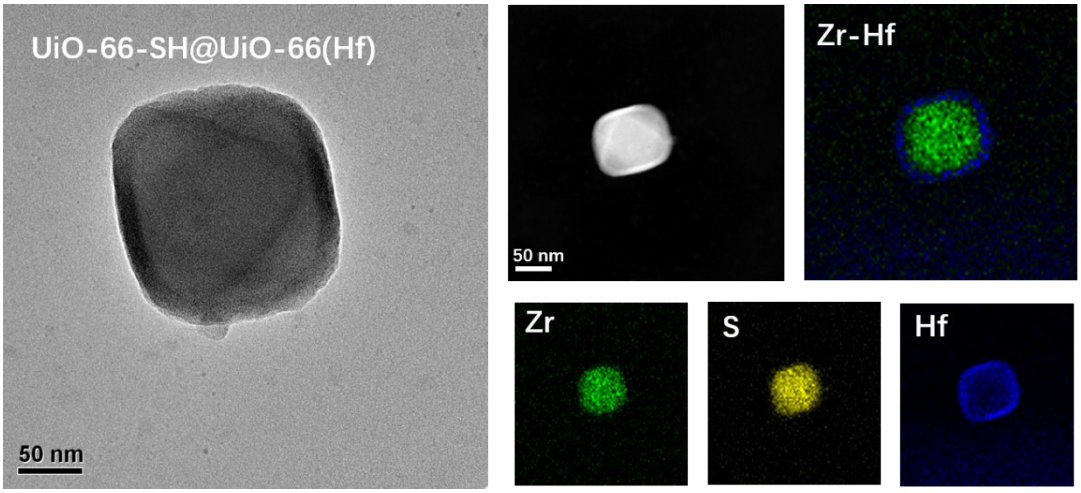

Figure S24. High-angle annular dark-field image and EDX mapping of Zr (green), S (yellow) and Hf (navy blue) in UiO-66-SH@UiO-66(Hf).

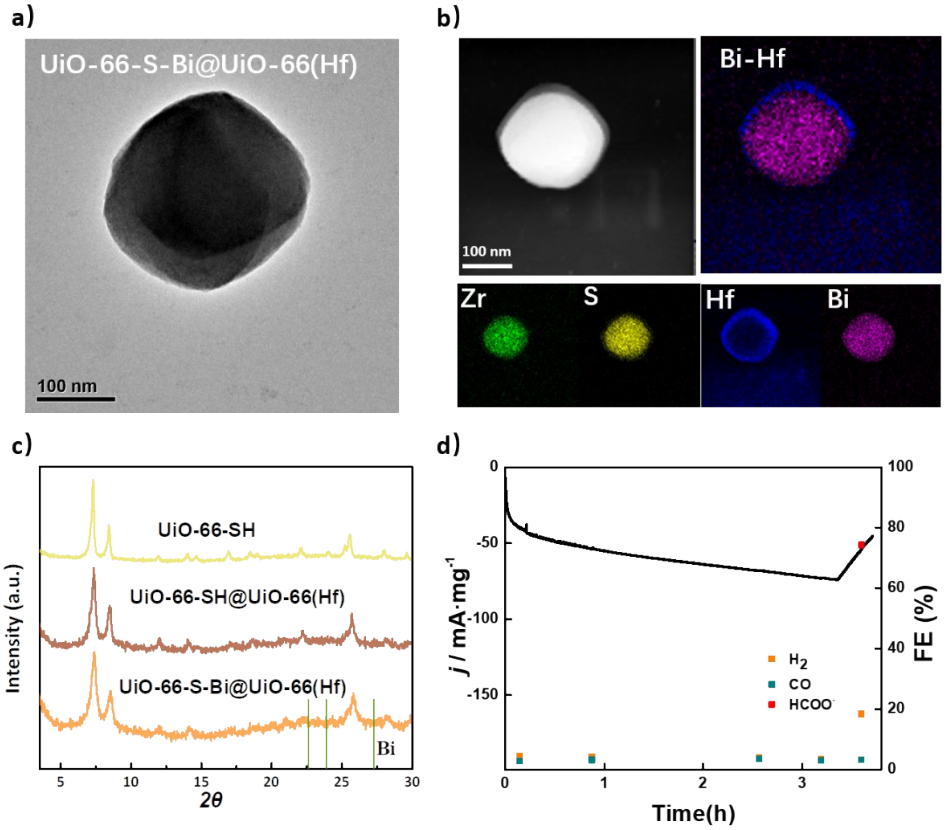

Figure S25. a) TEM images of UiO-66-S-Bi@UiO-66(Hf). b) High-angle annular dark-field image (HAADF) and EDX mapping of Zr (green), S (yellow), Hf (navy blue) and Bi (magenta) in UiO-66-S-Bi@UiO-66(Hf). c) PXRD patterns of the UiO-66-SH, UiO-66-SH@UiO-66(Hf) and UiO-66-S-Bi@UiO-66(Hf). d) Long-term electrocatalytic CO_2 reduction performance of UiO-66-S-Bi@UiO-66(Hf) in CO_2-saturated 0.1 M $KHCO_3$ electrolyte at -1.1 V *vs.* RHE.

4. Modelling voltage drop due to electrical resistance within the MOF

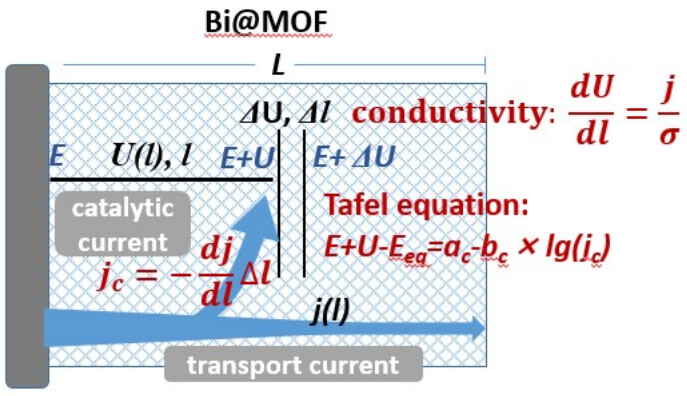

Figure S26. Analysis of the transport current j, catalytic current j_c, and voltage drop due to resistance U

The transport current density at the position l is $j(l)$.

The voltage drop due to MOF resistance at the position l is $U(l)$

Based on the definition of conductivity σ, we can obtain

$$\frac{dU}{dl} = \frac{j}{\sigma}$$

The catalytic current density that corresponds to the electron transfer from the catalytic centers to the substrate in the solution is $j_c = -\frac{dj}{dl}\Delta l$

The catalytic current density is determined by the Tafel equation in the high overpotential regime in electrolysis:

$$E + U(l) - E_{eq} = a_c - b_c \times lg[j_c(l)]$$

where E is the electrode potential, E_{eq} is the thermodynamic equilibrium potential, and b_c is the Tafel slope.

At l=0, we know $U(0)$=0,

So $E - E_{eq} = a_c - b_c \times lg[j_c(0)]$

Subtracting this from the expression at l, we can obtain

$$U(l) = -b_c \times lg[j_c(l)/j_c(0)]$$

or

$$j_c(l) = j_c(0)e^{-\frac{2.303\,U(l)}{b_c}}$$

Let $-\frac{dj}{dl}|_{l=0} = i_0$

$$\frac{dj}{dl} = -i_0 e^{-\frac{2.303\,U(l)}{b_c}}$$

Or

$$\frac{d^2U}{dl^2} = -\frac{i_0}{\sigma}e^{-\frac{2.303\,U}{b_c}}$$

with boundary conditions:

$$U(0) = 0$$

$$\frac{dU}{dl}|_{l=0} = \frac{j(0)}{\sigma}$$

$$\frac{dU}{dl}|_{l=L} = 0$$

Note that here we ignored the effect of double layer capacity because we are only interested in the steady state electrolysis in which capacity only has a minor effect.

Let

$$\gamma = \frac{l}{L}$$

$$\mho = \frac{2.303}{b_c}U$$

$$\alpha = \frac{2.303 i_0 L^2}{b_c \sigma}$$

$$\beta = \frac{2.303L}{b_c\sigma} j(0)$$

to obtain a unitless equation for numerical solution

$$\frac{d^2\tilde{U}}{dl^2} = -\alpha e^{-\tilde{U}}$$

with boundary conditions:

$$\tilde{U}(0) = 0$$

$$\frac{d\tilde{U}}{dl}\Big|_{l=0} = \beta$$

$$\frac{d\tilde{U}}{dl}\Big|_{l=1} = 0$$

There are two parameters α and β. β can be obtained from the experimentally observed total current I, electrochemical surface area (ECSA), MOF conductivity σ, Tafel slope b_c, and MOF thickness L by

$$\beta = \frac{2.303L}{b_c\sigma} \frac{j}{roughness\ factor}$$

Numerical solution of the differential equation found that in order to fulfill the boundary conditions $\alpha \approx 2.5175$

A relationship between the spatial distribution of the voltage drop $U(l)$ and the geometrical current density j can be obtained as shown in Figure 4d.

Matlab code for numerically solving the equation:

```
function [endderivative] = endderivative(alpha,beta,N)
    dl=1/N;
    U=zeros(N,1);
    dU=zeros(N,1);
    ddU=zeros(N,1);
    U(1)=0;
    ddU(1)=-alpha*exp(-U(1));
    dU(1)=beta;
    for i = 1:N-1
        dU(i+1)=dU(i)+ddU(i)*dl;
        U(i+1)=U(i)+dU(i)*dl;
        ddU(i+1)=-alpha*U(i+1);
    end
    endderivative=dU(end);
end

function [U] = VoltageDistribute(alpha,beta,N)
    dl=1/N;
```

```
    U=zeros(N,1);
    dU=zeros(N,1);
    ddU=zeros(N,1);
    U(1)=0;
    ddU(1)=-alpha*exp(-U(1));
    dU(1)=beta;
    for i = 1:N-1
        dU(i+1)=dU(i)+ddU(i)*dl;
        U(i+1)=U(i)+dU(i)*dl;
        ddU(i+1)=-alpha*U(i+1);
    end
end

Totalcurrentdensity=[1,3,5,10,20,50];%mA/cm2, 1,3,5,10,20,50 for the H cell
and 100,120 for the flow cell
roughnessfactor=4.95; % 4.95 for the H cell and 3.07 for the flow cell
bc=155;%mV/decade, Tafel slope
conductivity=10^(-6);%S/cm
MOFthickness=70;%nm
betalist=2.303*Totalcurrentdensity/roughnessfactor*10^(-
3)*MOFthickness*10^(-7)/(bc*10^(-3)*conductivity);
N=100;
l=(1:N)/N;
%determining alpha
for j=1:length(betalist)
    beta=betalist(j);
    f=@(alpha) endderivative(alpha,beta,N);
    alpha=fsolve(f,beta);
    fprintf(strcat('alpha:',num2str(alpha),'\n'))
    fprintf(strcat('beta:',num2str(beta),'\n'))

fprintf(strcat('zeropointerror',num2str(endderivative(alpha,beta,N)),'\n'))
end

%plot relationship between U(l) and current density
figure(1)
title('Voltage drops under different current densities')
xlabel('Distance from electrode / nm')
ylabel('Voltage drop due to resistance / mV')
hold on;
alpha=2.5175;
voltagedrop=zeros(length(betalist),N);
for j=1:length(betalist)
    beta=betalist(j);
```

```
    U=VoltageDistribute(alpha,beta,N);
    voltagedrop(j,:)=U*bc/2.303;
    plot(l *MOFthickness,U*bc/2.303);
end
for j = 1:length(betalist)
    leg_str{j} = [strcat(num2str(Totalcurrentdensity(j)),' mA/cm^{2}')];
end
legend(leg_str)
```

5. Stability of the electrolysis

Right now, the catalytic stability is one major concern of the Bi CO_2RR systems. Similar to what we observed in this work, the CO_2RR activity of most of the reported Bi catalysts underwent a sudden drop after electrolysis of several hours with only a few exceptions.[1-4]

To figure out the reason of the loss of activity, we performed further tests. After the catalytic activity of the UiO-66-S-Bi was lost, we renewed the cathode electrolyte solution to remove any potential poisoning species in the solution generated during the electrolysis, meanwhile the catalysts were exposed to air. This operation regenerates the activity (Figure S27a). In order to determine whether formate poisoned the catalyst, we added HCOONa (the same amount of formate produced in long-term electrolysis) before the activity drop. We found that the FE-$HCOO^-$ maintained, ruling out the poisoning by the formate product (Figure S27b).

On the other hand, if the deactivated UiO-66-S-Bi catalyst was taken out of the solution and exposed to air for 15 h without changing the electrolyte solution, the activity was regenerated (Figure S28a). Similarly, treatment of the UiO-66-S-Bi catalyst by an oxidative potential (1.0 V *vs.* RHE) can also partially regenerate the activity (Figure S28b). We thus conclude that some oxidative form of the Bi species is critical for the CO_2RR activity.

Besides, QiLong Zhu and coworkers found that renewing anode and cathode electrolyte after a period of electrolysis could extend the operation time.[5] In Figure S27a renewing the cathode electrolyte is effective to regenerate activity, so we just renewed anode electrolyte after *j* rapidly decreased to one fourth of the maximum value (Figure S29). In the first two times, the activity was effectively regained, while subsequent renewing anode electrolyte did not regenerate activity. Then the deactivated UiO-66-S-Bi catalyst was taken out of the electrolyte and exposed to air for 15h, the cathode electrolyte solution was also renewed, and the activity was regenerated, indicating that some oxidative form of the Bi species is critical for formate generation.

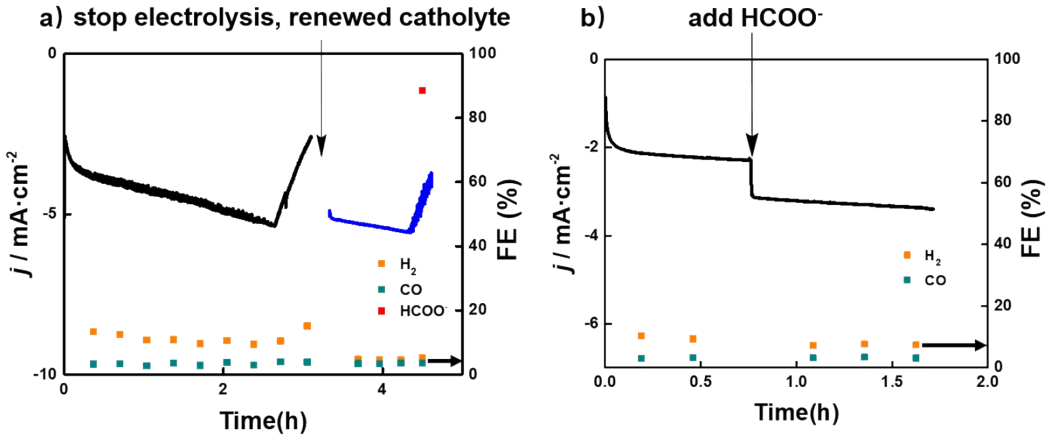

Figure S27. In the process of long-term electrocatalytic CO_2 reduction by UiO-66-S-Bi: a) Stopping electrolysis and renewing the cathode electrolyte after *j* rapidly decreased. b) Adding HCOONa before the *j* rapidly decreased.

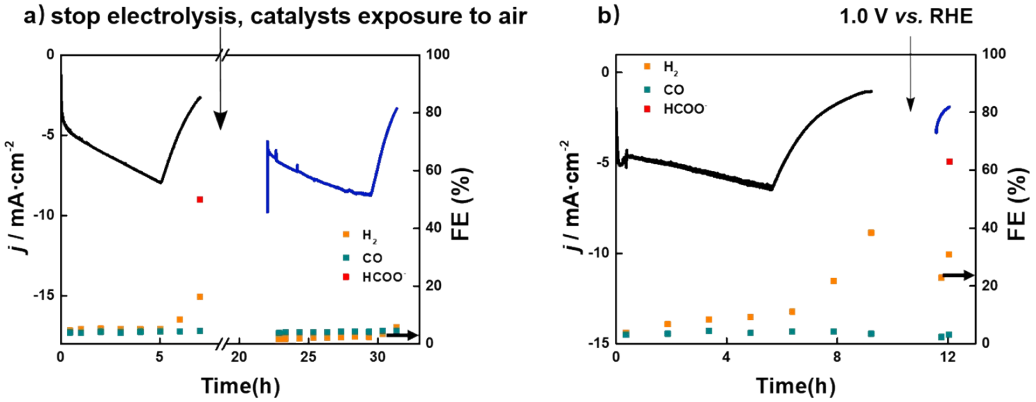

Figure S28. In the process of long-term electrocatalytic CO_2 reduction by UiO-66-S-Bi: a) After *j* rapidly decreased, stopping electrolysis and exposing the catalyst to air without renewing the electrolyte. b) After *j* rapidly decreased, changing voltage to 1.0 V *vs.* RHE (Figure 14 shows that the oxidation potential of Bi was 0.56 V *vs.* RHE), then measuring the CO_2 reduction performance (without renewing electrolyte and flowing CO_2).

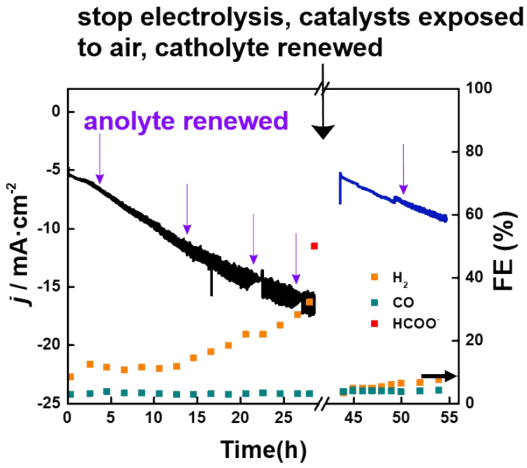

Figure S29. In the process of long-term electrocatalytic CO_2 reduction by UiO-66-S-Bi, renewing the anode electrolyte (the purple arrow) until the FE-H_2 increased, then stopping electrolysis, exposing the catalyst to air and renewing the cathode electrolyte.

Table 1. Comparison of CO_2RR catalytic performance of different Bi-based catalysts in flow cell.

Catalyst	Electrolyte	Current density (mA cm^{-2})	Current density (A mg^{-1})	Potential (V *vs.* RHE）	FE-formate (%)	Ref.
BiOBr-templated	2 M $KHCO_3$	200		-0.8	90	6
nanotube-derived Bi	1 M $KHCO_3$	140		-0.85	95	7
Bi_2O_3@C-800	1 M KOH	150		-0.9	93	8
Bi-ene	1 M $KHCO_3$	100		-1.08	99.6	9
Bi-ene-NW	1 M $KHCO_3$	200		ca. -1.2	90	10
$Bi_{0.1}Sn$	1 M $KHCO_3$ and KOH (pH=11）	100		-1	95	11
C-Bi RDs	1 M KOH	200		-0.68	＞86	12
Bi_2O_3/MOL	1 M $KHCO_3$	330		-1.16	＞80	13
Bi_2O_3/BiO_2	0.5 M $KHCO_3$	110		-1.2	95	14
EOD Bi	0.5 M $KHCO_3$	8.3	0.0083	-0.92	75	15

Bi LNSs	1 M $KHCO_3$		0.59	-1.1	92.2	[16]
UiO-66-S-Bi	0.1 M $KHCO_3$ + 0.9 M KCl	123	2.2	-1.1	88.5	this work

References

1. W. Zhang, S. Yang, M. Jiang, Y. Hu, C. Hu, X. Zhang and Z. Jin, *Nano Lett.*, 2021.
2. Y. Wang, L. Cheng, J. Liu, C. Xiao, B. Zhang, Q. Xiong, T. Zhang, Z. Jiang, H. Jiang, Y. Zhu, Y. Li and C. Li, *ChemElectroChem*, 2020, **7**, 2864-2868.
3. X. Zhang, J. Fu, Y. Liu, X.-D. Zhou and J. Qiao, *ACS Sustainable Chem. Eng.*, 2020, **8**, 4871-4876.
4. T. Fan, W. Ma, M. Xie, H. Liu, J. Zhang, S. Yang, P. Huang, Y. Dong, Z. Chen and X. Yi, *Cell Reports Physical Science*, 2021, **2**, 100353.
5. M. Zhang, W. Wei, S. Zhou, D.-D. Ma, A. Cao, X. Wu and Q.-L. Zhu, *Energy & Environmental Science*, 2021.
6. F. P. Garcia de Arquer, O. S. Bushuyev, P. De Luna, C. T. Dinh, A. Seifitokaldani, M. I. Saidaminov, C. S. Tan, L. N. Quan, A. Proppe, M. G. Kibria, S. O. Kelley, D. Sinton and E. H. Sargent, *Adv. Mater.*, 2018, **30**, e1802858.
7. Q. Gong, P. Ding, M. Xu, X. Zhu, M. Wang, J. Deng, Q. Ma, N. Han, Y. Zhu, J. Lu, Z. Feng, Y. Li, W. Zhou and Y. Li, *Nat. Commun.*, 2019, **10**, 2807.
8. P. Deng, F. Yang, Z. Wang, S. Chen, Y. Zhou, S. Zaman and B. Y. Xia, *Angew. Chem. Int. Ed.*, 2020, **59**, 10807-10813.
9. C. Cao, D.-D. Ma, J.-F. Gu, X. Xie, G. Zeng, X. Li, S.-G. Han, Q.-L. Zhu, X.-T. Wu and Q. Xu, *Angew. Chem. Int. Ed.*, 2020, **59**, 15014-15020.
10. M. Zhang, W. Wei, S. Zhou, D.-D. Ma, A. Cao, X.-T. Wu and Q.-L. Zhu, *Energy & Environmental Science*, 2021, **14**, 4998-5008.
11. L. Li, A. Ozden, S. Guo, F. P. García de Arquer, C. Wang, M. Zhang, J. Zhang, H. Jiang, W. Wang, H. Dong, D. Sinton, E. H. Sargent and M. Zhong, *Nat. Commun.*, 2021, **12**, 5223.
12. H. Xie, T. Zhang, R. Xie, Z. Hou, X. Ji, Y. Pang, S. Chen, M.-M. Titirici, H. Weng and G. Chai, *Adv. Mater.*, 2021, **33**, 2008373.
13. H. Liu, H. Wang, Q. Song, K. Küster, U. Starke, P. A. van Aken and E. Klemm, *Angew. Chem. Int. Ed.*, 2022, **61**, e202117058.
14. X. Feng, H. Zou, R. Zheng, W. Wei, R. Wang, W. Zou, G. Lim, J. Hong, L. Duan and H. Chen, *Nano Lett.*, 2022, **22**, 1656-1664.
15. E. Bertin, S. Garbarino, C. Roy, S. Kazemi and D. Guay, *J. CO2 Util.*, 2017, **19**, 276-283.
16. D. Wang, C. Liu, Y. Zhang, Y. Wang, Z. Wang, D. Ding, Y. Cui, X. Zhu, C. Pan, Y. Lou, F. Li, Y. Zhu and Y. Zhang, *Small*, 2021, **17**, 2100602.